Additive Manufacturing 89 (2024) 104286

Contents lists available at ScienceDirect

Additive Manufacturing

journal homepage: www.elsevier.com/locate/addma

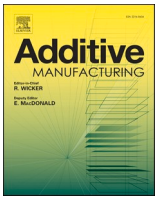

Elucidating the challenges in the development and deployment of refractory complex concentrated alloys for additive manufacturing

Magesh Kumaravel [a], Yazdan Eynolghozzat [a], Joachim Gussone [b], Fuyao Yan [c], Amir Ardeshiri Lordejani [a], Jan Haubrich [b], Guillermo Requena [b,d], Ida S. Berglund [c], Mario Guagliano [a], Sara Bagherifard [a,*]

[a] Politecnico di Milano, Department of Mechanical Engineering, Milan, Italy
[b] German Aerospace Center, Institute of Materials Research, Cologne, Germany
[c] QuesTek Europe AB, Solna, Sweden
[d] RWTH Aachen University, Aachen, Germany

ARTICLE INFO

Keywords:
High entropy alloys
Cold spray
Laser powder bed fusion
Processability

ABSTRACT

The increasing demand for advanced materials with load-bearing capabilities in extremely high-temperature environments has brought considerable attention to the design and fabrication of novel refractory complex concentrated alloys. Despite the notable progress in design of customized alloys, there are still significant challenges regarding their processing and fabrication, highly limiting their exploitation. In this study, model non-equiatomic Nb-Ta based refractory complex concentrated alloys were created as potential materials with improved high-temperature stability and performance for space propulsion applications. Gas atomization was used for producing spherical pre-alloyed powders. Two different additive manufacturing techniques, i.e., laser powder bed fusion and cold spray were used to explore the manufacturing complexities of this novel alloy. The results highlight the importance of powder's features on its processability by laser powder bed fusion and cold spray. High interstitial content, inhomogeneous microstructures, fractured and hollow particles, and the presence of microsegregation, led to embrittlement, and in case of cold spray, the wide particle size range of the feedstock resulted in undesired flowability, adversely affecting the processibility of the developed material. The obtained results provide valuable insights and recommendation for improving design, preparation, and fabrication of custom-designed refractory alloys for additive manufacturing.

1. Introduction

Increasing the operating temperatures of metallic materials, exceeding that of the state-of-the-art Nb-based C103 alloy and Ni-based superalloys, is desirable for a range of advanced applications at elevated temperatures, such as space and aerospace engines, gas turbine engines, hypersonic flight, etc. However, it remains a persistent challenge due to the trade-off between high-temperature strength and room-temperature ductility of the materials, which also limits their manufacturability [1–3]. The aim is development of new materials that can be easily made into feedstocks and reliably processed via additive manufacturing (AM) methods, which are increasingly used to manufacture geometrically complex load-bearing parts for aerospace applications, such as internally cooled turbine blades in gas turbines or for space engines [4].

In recent years, the field of refractory complex concentrated alloys (RCCA), including refractory high entropy alloys (HEAs), has given metallurgists more freedom in the alloying strategy to develop robust materials for extreme high temperature conditions that traditional alloys cannot withstand. Since the development of the first equiatomic TiZrHfNbTa and WNbMoTa RCCAs with high deformation potential [5,6], considerable progress has been made in exploring and designing non-equiatomic RCCAs within vast multi-dimensional compositional spaces. This progress is further substantiated by the development of high-throughput computational and experimental screening approaches aimed at improving the high temperature stability and ductility boundaries of materials [7–9]. Despite these unprecedented opportunities, RCCA are still a primitive alloy group facing development challenges, primarily owing to the intrinsic limitations in preparation of refractory materials combined with their processing complexities [10,11].

The high melting points of principal alloying elements in RCCAs

* Corresponding author.
E-mail address: sara.bagherifard@polimi.it (S. Bagherifard).

https://doi.org/10.1016/j.addma.2024.104286
Received 26 February 2024; Received in revised form 5 June 2024; Accepted 28 June 2024
Available online 1 July 2024

Nomenclature

AM	Additive manufacturing
ASTM	American Society for testing and materials
BCC	Body centered cubic
CCA	Complex concentrated alloys
CGHE	Carrier gas hot extraction
CS	Cold spray
DBTT	Ductile to brittle transition temperature
DED	Direct energy deposition
EBSD	Electron backscatter diffraction
EDS	Energy dispersive X-ray spectroscopy
EIGA	Electrode inert gas atomization
FCC	Face centered cubic
HEA	High entropy alloys
HT-LPBF	High temperature laser powder bed fusion
IPF	Inverse pole figure
KAM	Kernel average misorientation
LPBF	Laser powder bed fusion
LT-LPBF	Low temperature laser powder bed fusion
RCCA	Refractory complex concentrated alloys
SEM	Scanning electron microscopy
XRD	X-ray diffraction

makes it challenging to achieve homogeneous microstructures. Still in most studies, alloying of RCCAs is commonly achieved by melting. Considering the high affinity of refractory metals to oxygen, the melting process needs to be carried out in vacuum or a high-purity inert atmosphere. Vacuum arc melting is the most common approach to prepare lab-scale RCCA bulk samples. This process requires multiple re-melting steps to ensure the homogeneity of the melt. With sufficient and well-controlled homogenization treatments to remove microsegragations and phase separations induced by solidification, promising mechanical properties have been achieved for some RCCAs [12]. Alloying using high-energy methods beam melting, such as electron or laser beams, is an attractive method for preparing RCCAs. This technique offers the advantage of minimal microsegregation due to the rapid solidification process. Using AM technologies allows to exploit *in-situ* alloying from elemental powders during fabrication, which can accelerate the alloy development. Most of the available studies have been focused on direct energy deposition (DED) technologies. For instance, Dobbelstein et al. produced MoNbTaW [13] and TiZrNbHfTa [14] RCCA samples via *in-situ* alloying, through DED of elementary powder blends. However, due to the large melting point differences between elemental materials, re-melting had to be applied. In addition, DED has been used as a high-throughput fabrication method for composition screening, e.g., within the MoNbTaW [15] and the TiZrNbTa systems [16]. Processing strategies for *in-situ* alloying have also been developed for laser powder bed fusion (LPBF). Huber et al. investigated *in-situ* synthesis of equiatomic WMoTaNbV by direct use of the pre-mixed powder blend in the powder bed for LPBF [17]. While they could achieve single-phase BCC structure, undissolved W particles and microcracks could not be avoided. Similar results were obtained for the same powder blend composition by Ron et al. [18] and Zhang et al. [19].

The state-of-the-art underlines that achieving a homogenous elemental distribution and complete melting of the powder particles in a system of alloying elements with widely varying melting points is extremely challenging. Therefore, an AM-based fabrication strategy employing pre-alloyed powders can be more promising for obtaining reproducible homogeneous materials, which may entail their own additional process-specific complexities. In the case of AM technologies which use high-energy beams, such as LPBF and DED, materials experience large thermal gradients and rapid solidification rates, necessitating high processing robustness to resist solidification and stress-related cracking problems [20]. On the other hand, for solid-state AM methods, particularly CS, where the process entails accelerating the metallic powder to a supersonic velocity through a convergent divergent nozzle, deposition quality is governed by the severe plastic deformation of the particles upon impacting the substrate [21]. Successful bonding takes place when the velocity of the particle is higher than a critical velocity, which depends on the thermo-mechanical properties of the powder [22].

There are limited studies on implementing AM for pre-alloyed RCCA. One report of successful LPBF processing of $Ti_{1.4}Nb_{0.6}Ta_{0.6}Zr_{1.4}Mo_{0.6}$ RCCA involved using pre-alloyed powders produced by electrode induction heating inert gas atomization (EIGA) [23]. The uptake of interstitial impurities (e.g., O and N) during powder atomization and processing was identified as a characteristic of AM processing compared to conventional production routes. For instance, oxygen and nitrogen concentrations observed in as-atomized steel powders were higher by about one order of magnitude compared to a conventionally produced ingot, as reported in many studies (e.g., [24]). This uptake becomes more critical for refractory alloys, and especially RCCA, which can be significantly embrittled by interstitial elements. It was reported by Barnett et al. [25] that blended feedstock of Ta-10 W from pure Ta and W powders contained 8 times more oxygen than an extruded commercial tube, whereas the as-atomized powders exhibited 36 times more oxygen. This impeded cold spray deposition until additional deoxidation, and size classification steps were implemented. Various FCC-structured HEAs and CCAs [26–30] as well as BCC HEAs/CCAs such as AlCoCrFeNi [31], FeCoCrAlCu [32], AlCoCrCuFe [33], and AlNiCoFeCrTi [34] have been reported to be successfully deposited via CS process, in all cases as coatings with limited achievable thickness.

A key factor contributing to the scarcity of reports on AM of RCCAs using pre-alloyed powders is the significant challenge in producing high quality powder feedstock, i.e., homogeneously melted composition with low contaminant fractions such as oxygen or nitrogen. Gas atomization is a common and well-established method for producing spherical pre-alloyed powders, necessary for powder-based AM technologies. However, atomization of custom alloys at small to medium scales (up to some 10 kg), while principally being possible, is usually extraordinarily expensive and time-consuming. These constraints together with the imposed limitation of high melting temperatures of the constituent elements, decrease the production appeal of custom-designed refractory alloys or RCCA and result in very limited number of feedstocks vendors.

This work is driven by the limitations in thermal stability of incumbent Ni-based superalloys for in-space propulsion systems and is intended to assess the adoption of a novel RCCA in combination with different AM technologies, namely LPBF and CS. The goal is efficient use of critical raw materials and fabrication of seamless structures. In particular, the effects of alloy-intrinsic properties and production-induced powder features on their processability by various AM methods are analyzed and showcased by a model non-equiatomic RCCA alloy. To this aim, design, development, powder production, and processing properties by LPBF as well as CS are investigated for a RCCA consisting of the elemental range TaNbWTiVMoCr. This work aims to reduce the technical obstacles for practical applications of RCCA by elucidating the challenges associated with their processing and therefore to support and provide recommendations for the acceleration of their development and implementation. Understanding these challenges and implication will provide insights for RCCA development for AM and pave the way for filling the current technical gaps.

2. RCCA pre-alloyed powder production

A model non-equiatomic RCCA (Nb_1Ta_1 $W_{0.2}Ti_{0.5}V_{0.4}$ with minor addition of Mo and Cr), hereafter referred to as RCCA#1 was produced through electrode induction melting inert gas atomization (EIGA) process by TANiOBIS GmbH (DE).

The powder's flowability was checked using a Hall flowmeter funnel following ASTM B213–97; The results indicated a reproducible low flow time of ~ 8 s for 50 g of powder, indicating a very good flowability for AM. Scanning electron microscopy (SEM) analysis indicated mostly spherical powder particles surrounded by some satellite structures (Fig. 1a). In some cases, these sub-μm-sized satellite structures were detached and were identified as separate particles. SEM observations and particle size analysis performed with particle size analyser (Morphologi 4, Malvern panalytical Ltd) indicated a wide particle size range. The particles were embedded in a conductive resin, ground, and polished for SEM microstructural analysis. The measured volumetric size distribution values D10, D50, and D90 were evaluated equal to 17.98 μm, 48.89 μm and 72.26 μm, respectively. The number distribution analysis yielded a mean size of 7.19 μm for the feedstock with D10, D50 and D90 values of 1.04 μm, 4.02 μm, 15.76 μm, respectively, indicating a high density of small sized particles.

As evident in SEM images, many particles exhibit dendritic microstructural features induced by rapid solidification during powder atomization, while as indicated in Figs. 1b and 1d, a few contain large equiaxed solidification areas. The composition analysis of the cross-sections of those powder particles was conducted by energy dispersive X-ray spectroscopy (EDS). Fig. 2a shows qualitative EDS maps, demonstrating the inhomogeneous distribution of the elements in the powder. Fig. 2b illustrates the deviation of the Ta/W-enriched areas with respect to nominal composition, with the data taken from analysis of such enriched areas shown in Fig. 1b. As these values differ from particle to particle, the EDS measurements presented here can sufficiently demonstrate the observed variation. In addition, microsegragations of Ti, V and Cr are observable in the as-solidified interdendritic regions (Fig. 3b). The measured mean hardness of the powder particles, performed on their cross-sections, was equal to 502 ± 38 $HV_{0.025}$.

Based on a prediction using the classic Scheil model implemented in Thermo-Calc software version 2023b [35] along with TCHEA6 High Entropy Alloys database [36], the alloy is expected to solidify as BCC phase throughout a wide temperature range (Fig. 3a). Furthermore, this simulation allows for prediction of the elemental distribution across a dendrite, as depicted in Fig. 3b. It is predicted that Ti, V and Cr tend to segregate in the interdendritic regions, and the dendrite core tends to be enriched in Ta, W and Mo, which is in agreement with the experimental observation of elemental distributions, regardless of actual cooling rates. Using the carrier gas hot extraction (CGHE) methodology, the as-atomized powder was measured to contain ~1700 ppm oxygen and ~200 ppm nitrogen (by weight). As indicated by Belcher et al. [37], interstitial oxygen and nitrogen have a considerable interstitial

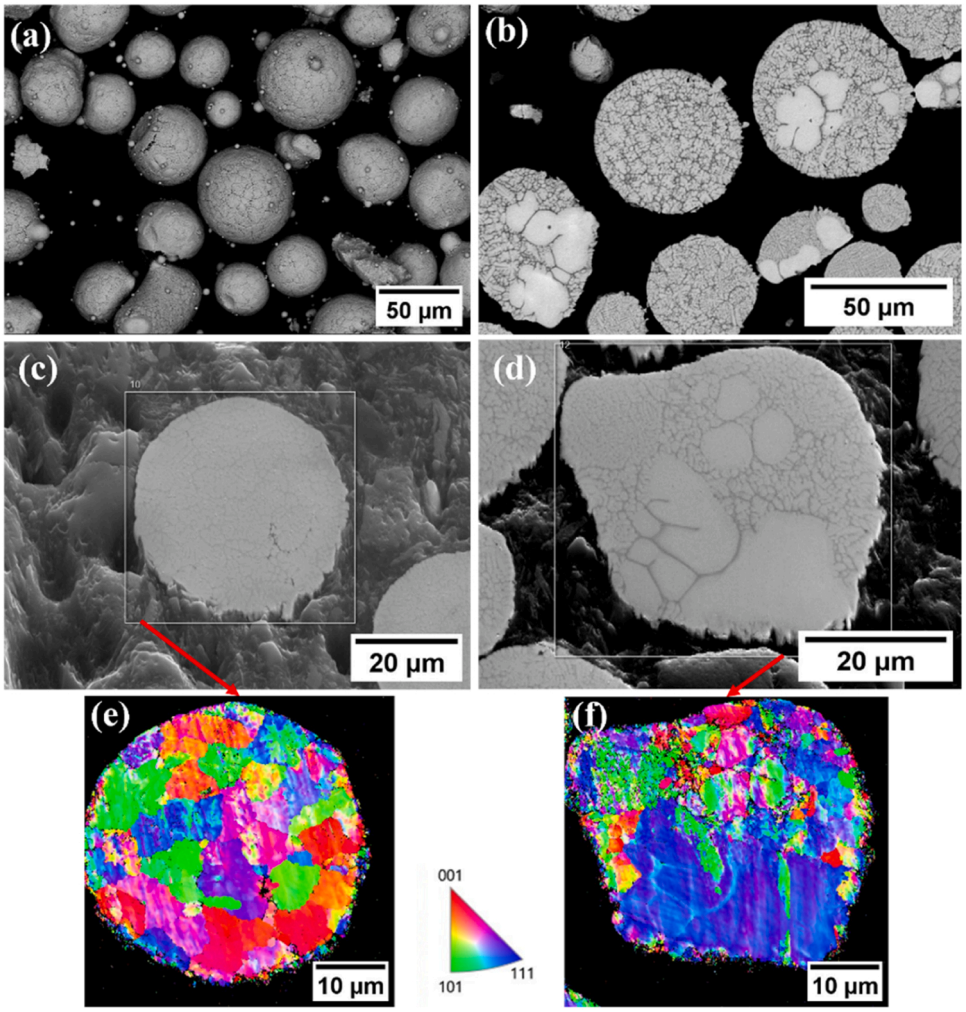

Fig. 1. (a) Morphology of RCCA#1 powder. (b) Cross-section of the powder particles. (c-d) Cross-section of single RCCA#1 particles; (e-f) the corresponding electron backscatter diffraction IPF maps.

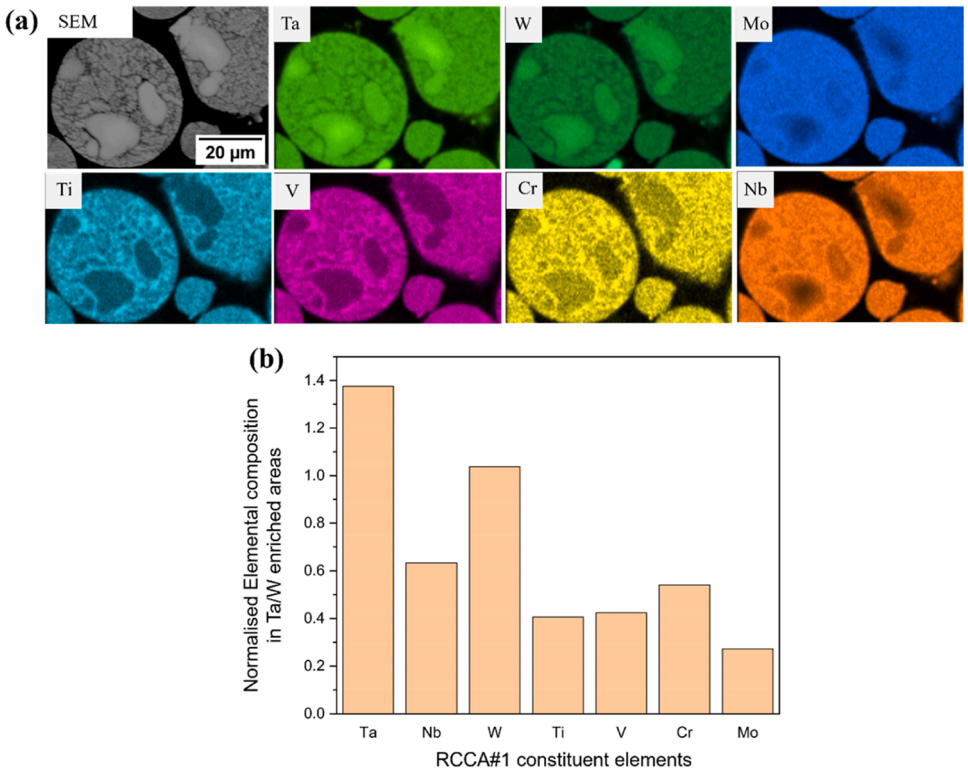

Fig. 2. (a) EDS elemental mapping of individual particles containing bulk areas enriched in Ta and W. (b) Chemical composition in the enriched areas from Fig. 1b, normalized with respect to the to the intended composition of the RCCA#1 powder.

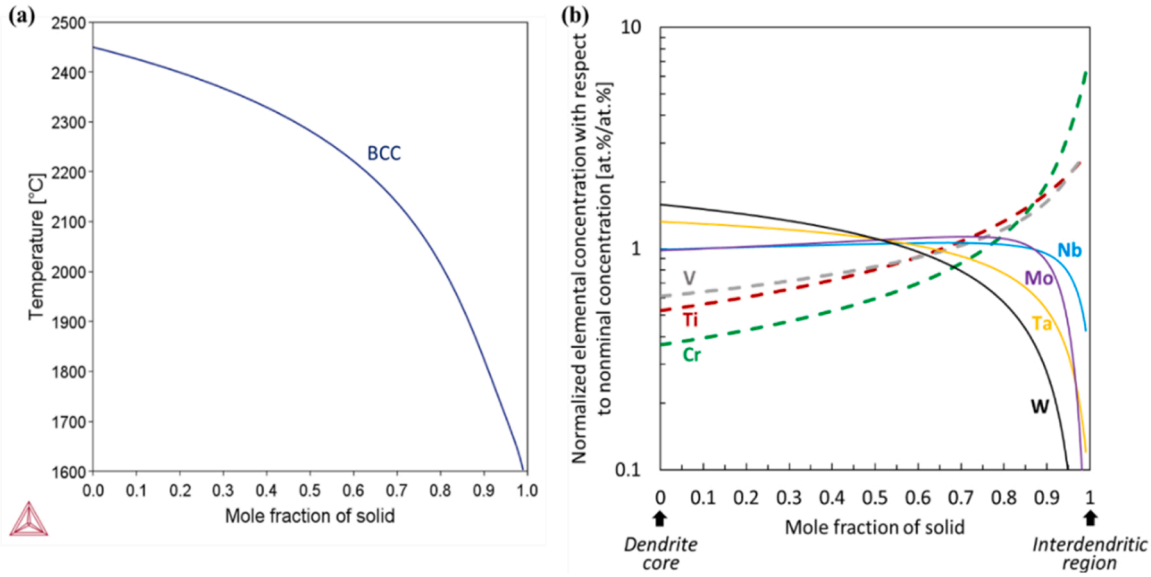

Fig. 3. (a) Classic Scheil solidification simulation of RCCA#1 alloy. (b) Predicted normalized elemental distribution across the dendritic structure (V, Ti and Cr curves are dashed to differentiate their segregating behaviors with the rest of the elements).

strengthening effect on subgroup V metals but can also cause detrimental embrittlement when they are above 1 at%, whereas trace amounts as low as 100 ppm can embrittle all subgroup VI elements. Therefore, it is reasonable to postulate a high likelihood of intrinsic brittleness of the as-atomized powders as also evidenced by signs of microcracks in some of the powder particles (examples shown in Fig. 1a).

3. LPBF processing

3.1. LPBF facility and process parameters

LPBF was carried out in an SLM Solutions 280^{HL} machine equipped with a 400 W Nd: YAG fibre laser under high-purity argon atmosphere (> 99.999 %). LPBF experiments were carried out using a build space reduction (50 × 50 mm^2) that has been constructed for small powder amounts. A gas purification system was integrated to further reduce

traces of O_2 and H_2O. The system was additionally equipped with a heating system that can heat the baseplate up to ~1200 °C. The substrate temperature was measured by a thermocouple attached at the side of baseplate, which for this study. was made of Ti-6Al-4 V Cuboid samples ($w \times l \times h = 5 \times 5 \times 12$ mm^3) were produced without and with pre-heating the baseplate to ~1000 °C. A simple pre-screening of process parameters was done with the main purpose of identifying the suitable set of parameters for manufacturability of these powders. The layer thickness (t) was set to 30 μm for all experiments and laser power (P) and the scanning rate (v) were varied from 200 to 300 W and 450–600 mm/s, respectively, using 2 hatch distances of $h = 0.1$ ($E_V = P/(h \bullet v \bullet t)$ 0.075 mm. Sample production, as indicated by [38], was carried out covering an energy density (EV = P / (h * v * t)) ranging between 139 J/mm^3 and 296 J/mm^3.

As presented below, these experiments with and without preheating indicated some limitations with RCCA#1 intrinsic properties and consequent great challenges in its production with the available LPBF system.

3.2. LPBF processing observations

The first LPBF trials were carried out without pre-heating the baseplate (low temperature, hereafter denoted as LT-LPBF). Samples were built up to more than 12 mm without any visually recognizable peculiarities. However, as shown in Fig. 4a and b, the final sample surfaces were covered with cracks extending over several melt tracks.

Furthermore, microscopic analyses of the cross-sections, quickly revealed extended crack networks (Fig. 5a and b) with crack densities ranging between 4 and 9 mm/mm^2. In addition, Fig. 5c and d clearly illustrate a high density of interdendritic shrinkage porosity.

To better understand the origin of the cracks, the samples were partially cut, and the remaining part was broken in a controlled manner such that internal fracture surfaces could be analyzed. The crack path showed intercrystalline and transcrystalline areas (Fig. 6a). Typical dendritic structures on inner surfaces indicated crack formation induced by hot tearing (Fig. 6b) [39–41]. The observation of dendrite/cellular structures has been reported at the fractured surfaces for superalloys [42] and high entropy alloys [43]. In agreement with the literature these structures can be attributed to solidification cracking / hot tearing.

The inter- and transcrystalline fracture patterns without dimples, in contrast, revealed the brittleness of the RCCA#1 alloy. As shown in Fig. 5, LPBF samples exhibited extended crack networks with crack densities up to 9 mm/mm^2 and SEM observations revealed dendritic structures within inner surfaces indicating solidification crack initiation (Fig. 6). Due to the material's brittleness, that is at least partially caused by the high interstitial contents, further crack growth, assisted by tensile residual stresses intrinsic of LPBF, could not be impeded. Furthermore, the bright areas (indicated by white arrows in Fig. 5a) suggest presence of un-melted particles, enriched in Ta and W which are maintained from the feedstock powders as reflected in Figs. 1d, 2 and 3.

3.2.1. LPBF processing at elevated temperatures

LPBF trials were also carried out with baseplate-heating at preheat temperatures of ~1000 °C (high temperature – hereby referred to as 'HT-LPBF') to reduce temperature gradients leading to residual stresses, which in conjunction with metallurgic solidification problems (e.g., residual melt in interdendritic regions) can lead to crack formation. Consequently, a significant reduction of crack densities to ~ 1 mm/mm^2 was observed. However, extended vertical cracks, i.e., those almost parallel to the build direction, were still present (Fig. 7a and b). The microstructure was coarser than that of LT-LPBF, with nano-sized platelet-like particles being observable within the interdendritic regions (Fig. 7c and d).

The nanoprecipitates were far too small for a quantitative evaluation by EDS in SEM. However, EDS line-scans revealed that the precipitates were enriched in Ti, with depletion of other elements (Fig. 8a). The line-scan in Fig. 8b also demonstrates the precipitates being located primarily in the interdendritic segregations.

The bulk composition of RCCA#1 both as powder and as LPBF printed part was measured by EDS, with compositional changes illustrated in Fig. 8c. The composition changes being small considering the limited accuracy of EDS, a slight weight loss is observable for Ti, V and Cr, as the elements with the lowest melting/boiling points. The amount of the interstitials O and N was determined by carrier gas hot extraction (CGHE). While the oxygen content was already very high in the powder (~ 1700 ppm) no oxygen pick-up was observable because of LPBF processing. Furthermore, there was a small reduction that may be explained by the evaporation of oxygen during the LPBF process (Fig. 8d), further intensified for the HT-LPBF sample. In contrast, there was virtually no change of the N content (~ 200 ppm) during LT-LPBF, whereas a strong increase to ~ 700 ppm occurred during HT-LPBF. These observations can be attributed to the high capacity of the gas purification system of the LPBF machine to reduce O and H_2O from the Ar inert gas atmosphere, while not being equipped to reduce the N content from the atmosphere.

The fractographic investigation of a purposefully broken HT-LPBF sample revealed inter- and transcrystalline cracks (Fig. 9a). Inner surfaces revealed dendritic structures similar to those of the LT-LPBF experiments (Fig. 6), highlighting the presence of hot tearing mechanism also for the HT-LPBF samples (Fig. 9b). Notably, on the intercrystalline surfaces there were small features (inset of Fig. 9a) that correspond to the nanoprecipitates observed in the microstructural investigation (Fig. 7d and Fig. 8a and b).

EBSD carried out at a cross-section close to the top surface of an HT-LPBF sample of RCCA#1 showed a large portion of the elongated grains with a preferred crystallographic orientation (Fig. 10a). The <100> fiber texture in the build direction (z) was confirmed by the corresponding pole figures (Fig. 10b).

The RCCA#1 alloy was designed with a single-phase BCC structure, which is widely confirmed by XRD (Fig. 10c). A close observation of the diffractograms, however, shows small reflections revealing minor

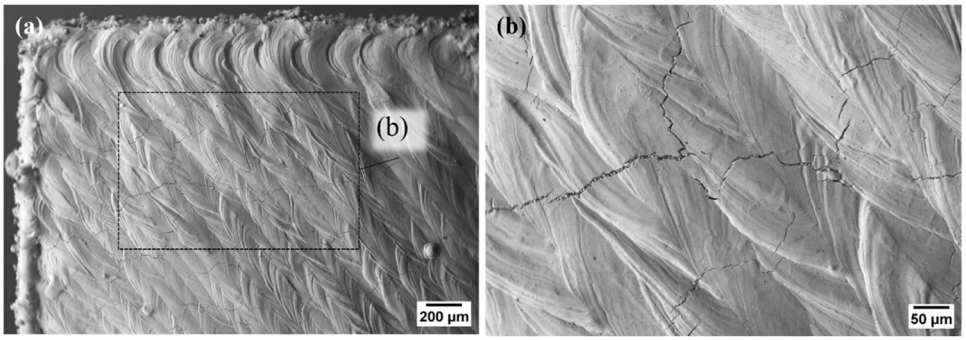

Fig. 4. SEM observations of RCCA#1 processed with LT-LPBF processed with P = 300 W, v = 450 mm/s, h=75 μm. (a) Top surface of the LPBF sample (b) Top surface zoomed in revealing cracks extending over several melt tracks.

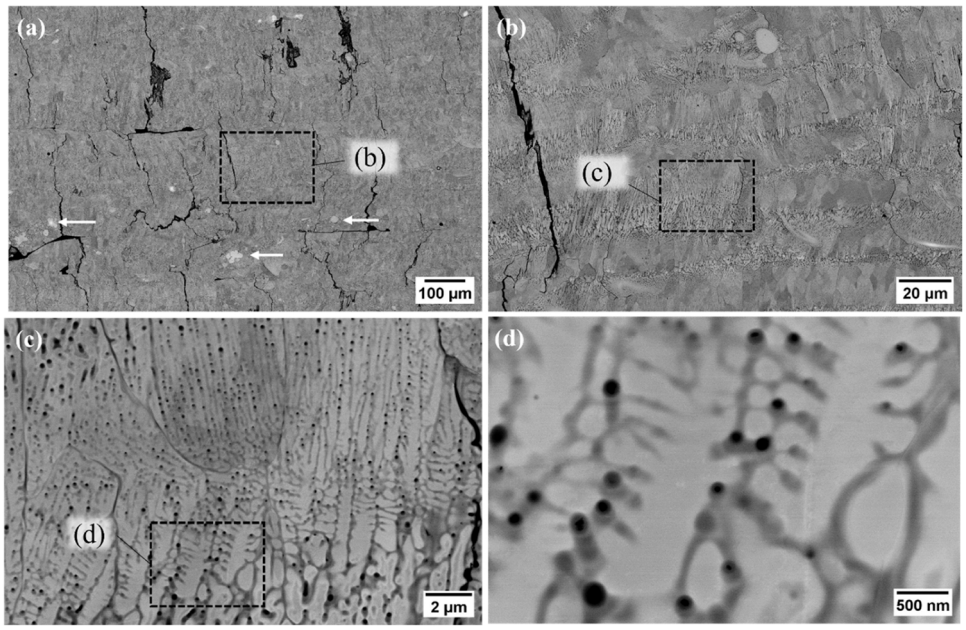

Fig. 5. SEM observations of RCCA#1 processed with LT-LPBF processed with P = 300 W, v = 450 mm/s, h=75 µm. (a, b) Intercrystalline and transcrystalline cracks. The white arrows indicate not fully molten W and Ta -rich areas (c, d) Interdendritic segregation and shrinkage porosity.

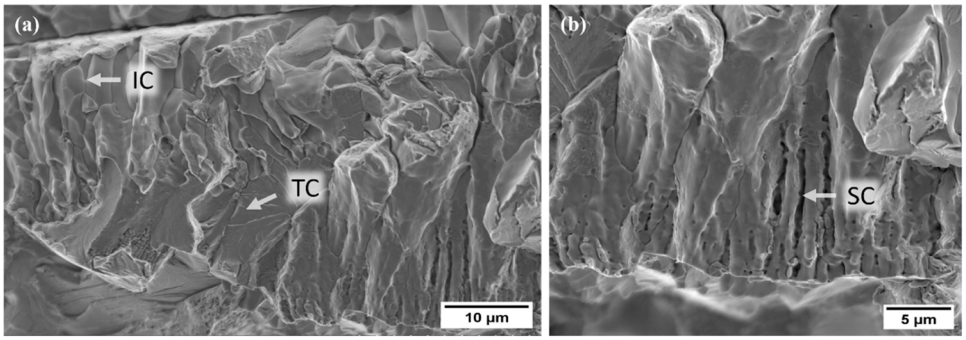

Fig. 6. SEM fractographic investigation of LPBF sample that was broken to reveal inner surfaces. (a) Intercystalline (IC) and transcrystalline (TC) fracture. (b) Dendritic structures indicating solidification cracking (SC).

amounts of additional phases (Fig. 10d). There is one reflection at $2\theta \approx 42^{\circ}$, which is observed in all diffractograms (including as-atomized powder and the LPBF) that could correspond to the 010 reflection of α-Ti (Fig. 10d). Additional reflections were identified for the HT-LPBF material, and the sintered power collected from the build plate after processing, which can be explained by the formation of TiN particles at elevated temperatures, i.e., the nanoprecipitates observable in Fig. 7d.

4. CS processing

4.1. CS facility and process parameters

Two substrate materials with distinct ranges of hardness were selected for CS deposition, namely Al alloy 6082-T6 (104 ± 2 $HV_{1.0}$) and Nimonic 75 (277 ± 9 $HV_{1.0}$). The dimensions of the Al 6082 T6 substrates were $25 \times 16 \times 5$ mm^3, whereas those of Nimonic 75 substrates were $25 \times 16 \times 3.15$ mm^3. The Nimonic 75 was selected as the substrate material due to its high hardness, promoting higher particle deformation upon impact.

The spray experiments were performed using high-pressure CS system (Impact innovations 5/8 system, DE) with Nitrogen as the process gas. CS process parameters were optimized after a few trials, with their final values listed in Table 1. In addition to full coatings, wipe tests, i.e. sprayings with high nozzle traverse speed and low powder feed rate, were conducted to achieve dispersedly deposited particles for accurate inspection of their bonding behavior with the substrate material. These experiments were conducted to inspect the individual splats, evaluate the mechanism of particle-substrate interfacial bonding, and analyze the feasibility of achieving thicker deposits on the given substrate materials. The thickness of the substrate was measured before and after each deposition.

4.2. CS processing observations

From wipe test results shown in Fig. 11, mechanical interlocking can be discerned as the predominant mechanism for bonding of RCCA#1 particles to the substrate. Surface observations of Al 6082 T6 substrate indicated low deformation of the interlocked particles with their initial shape highly retained upon impact, while the substrate underwent extreme plastic deformation with outward shearing (see Fig. 11a). Surface inspection on the Nimonic 75 substrate also indicated mechanical interlocking (Fig. 11b, c), albeit with negligible shearing of the substrate. A few cracked or broken particles were discernible (indicated by yellow arrows) in Figs. 12c or 11b, respectively. In both cases, there was no evidence of formation of material jetting at particle-substrate interface, suggesting the lack of metallurgical bonding between the

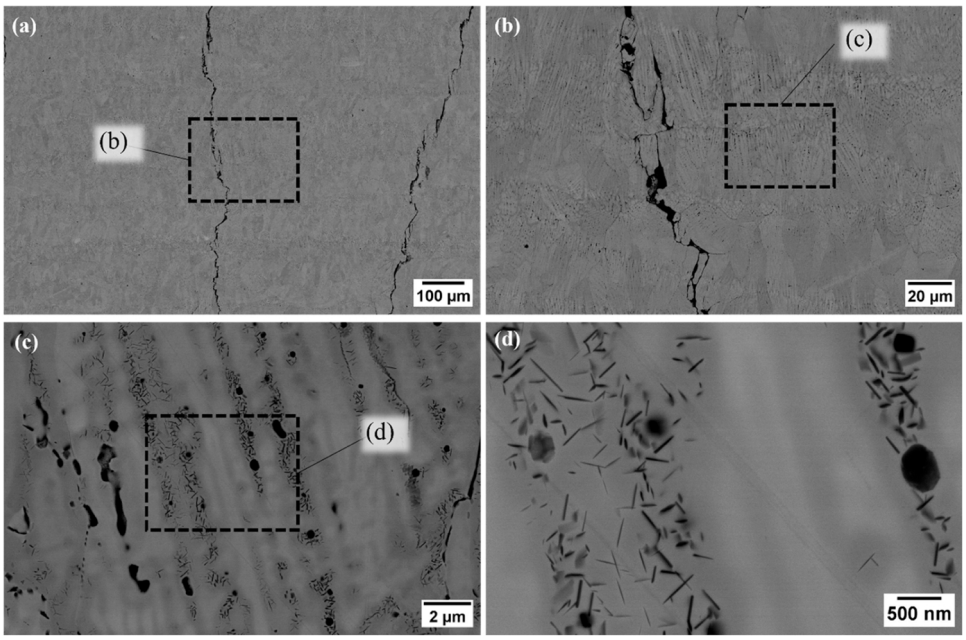

Fig. 7. SEM observation of RCCA#1 processed with HT-LPBF (P=300 W, v=450 mm/s, h=75 µm). (a, b) Large cracks parallel to build direction. (c) Interdendritc segregation and shrinkage porosity. (d) Nanoprecipitates within interdendric regions.

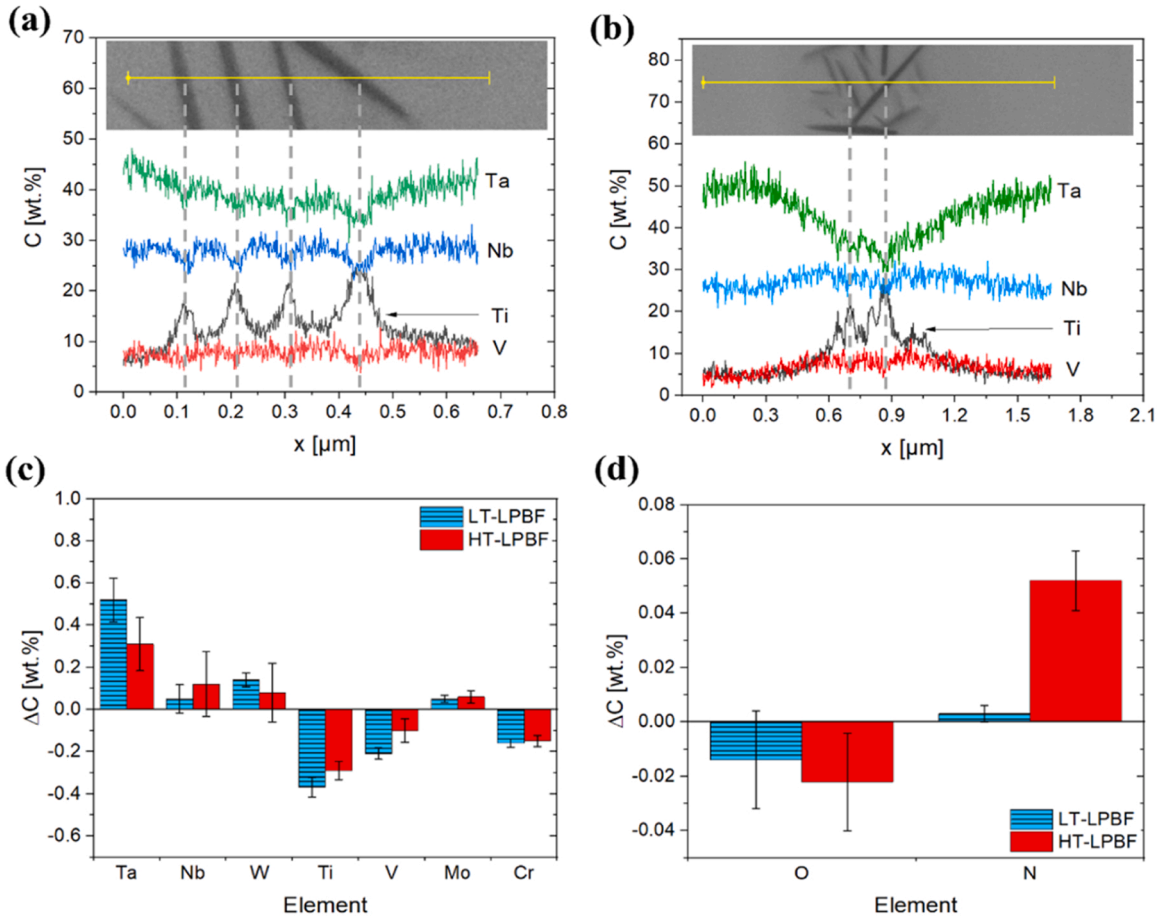

Fig. 8. EDS line-scans indicating the precipitates in the interdendritic regions of RCCA#1 processed with HT-LPBF. (a) Line-scan within interdendritic region. (b) Line-scan connecting two dendritic branches. (c) Compositional changes of RCCA#1 during LPBF processing as measured by EDS. (d) Compositional changes of the interstitials O and N as measured by CGHE.

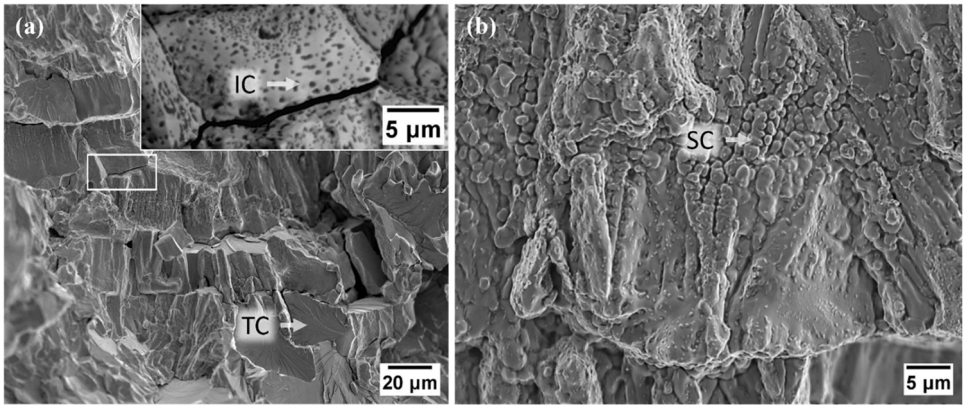

Fig. 9. Fractographic investigation of RCCA#1 processed with HT-LPBF. (a) Intercystalline (IC) and transcrystalline (TC) fracture with inset showing nano-precipitates on intercrystalline fracture surface. (b) Dendritic structures indicating solidification cracking (SC).

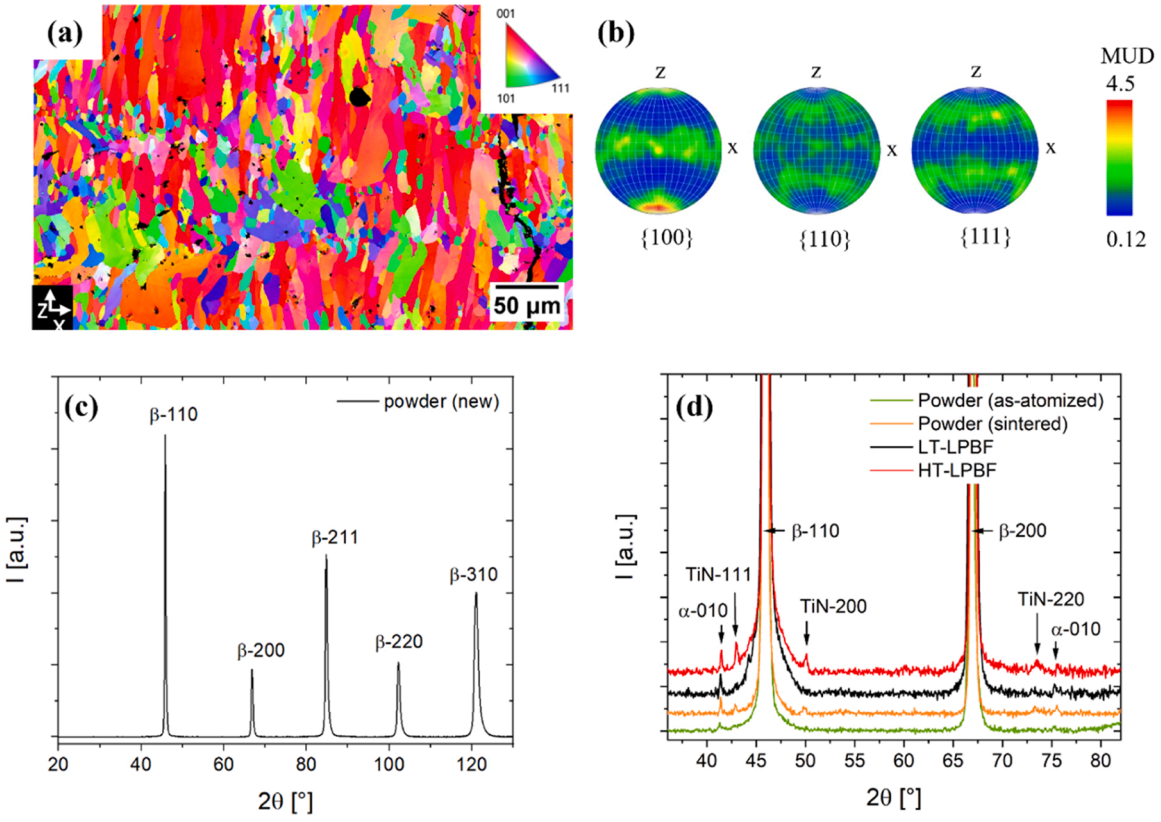

Fig. 10. EBSD investigation of RCCA#1 processed with HT-LPBF. (a) Inverse pole figure (IPF) mapping for build direction (z). (b)Pole figure showing <100> fiber texture. (c) XRD (Co-K_α radiation) diffractogram of RCCA#1 powder before LPBF experiments. (d) Comparison of diffractograms before and after LPBF processing to reveal very small reflections related to minor amounts of TiN and α-phase.

Table 1
CS process parameters.

Substrate material	Aluminum 6082 T6		Nimonic 75	
Spray strategy	Wipe test	Coating	Wipe test	Coating
Gas stagnation pressure (bar)	45	45	45	45
Gas stagnation temperature (°C)	750	750	800	800
Nozzle speed (mm/s)	800	333	600	60
Powder feed rate (g/min)	28	43	43	60
Step size (mm)	1	1	1	1
Stand-off distance (mm)	40	80	40	40
Number of layers	-	15	-	4

particles and the substrates.

As for the fully coated samples (achieved by 15 successive full-coverage scans), surface examination of the Al 6082 T6 substrate indicated partial coverage and sporadic deposition as illustrated in Fig. 12a. Upon analyzing the Nimonic 75 substrate, an even lower number of deposited particles were observed as discernible from Fig. 12c-e. Moreover, the high density of observable craters indicated that many particles rebounded after impacting the Nimonic 75 substrate. On both substrates, features of what seem to be zones of intermixing, composed of the RCCA#1 particles and the substrate material were observed. Both samples exhibited a very rough surface after cold spraying, which could have arisen from the high hardness of the RCCA#1 particles. In the case

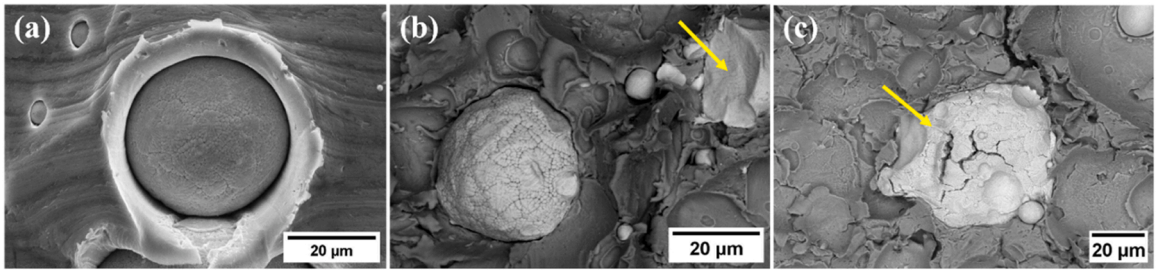

Fig. 11. SEM top-surface observation of wipe test samples. RCCA#1 sprayed on (a) Al 6082 T6 substrate (secondary electron (SE) image) and (b) Nimonic 75 substrate (Back scattered electron (BSE) image), both exhibiting mechanical interlocking. (c) Fractured particle upon impact on Nimonic 75 substrate (BSE) (yellow arrows indicating broken/cracked particles).

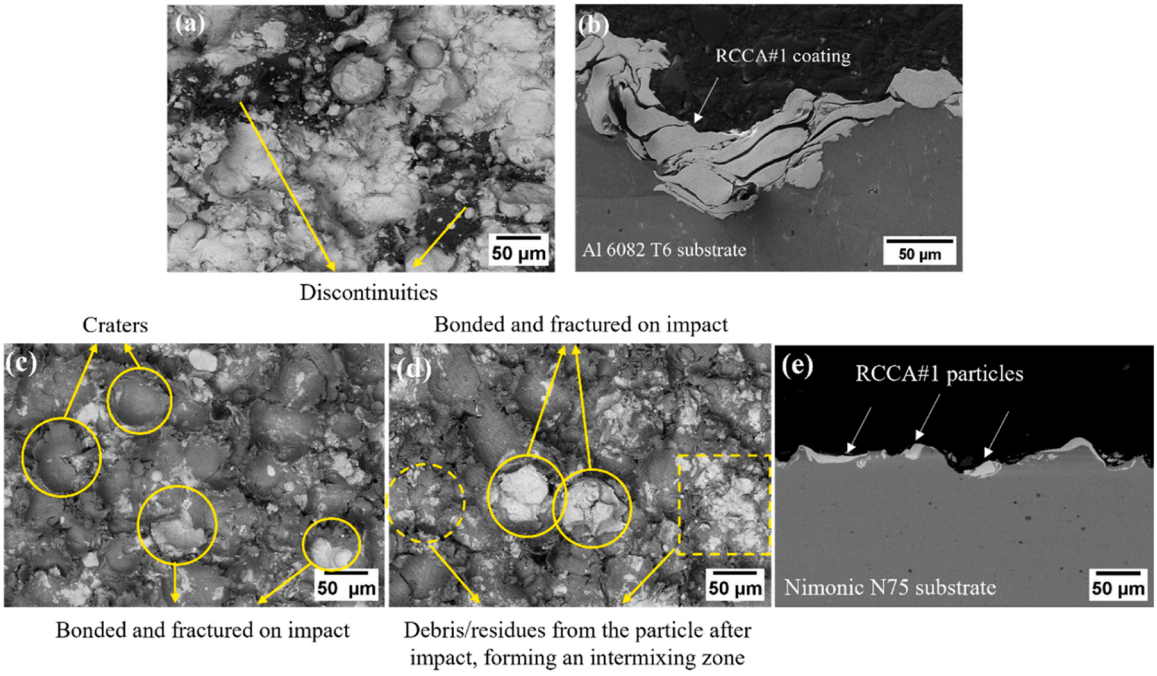

Fig. 12. SEM-BSE images of (a) Surface morphology showing discontinuities, (b)cross-section of RCCA#1 deposits on sprayed on Al 6082 T6 substrate. (c, d) Surface morphology showing the features of the deposit. (e) Cross-section RCCA#1 deposits sprayed on Nimonic 75.

of Al 6082 T6 substrate, the relative softness of the substrate with respect to the powder particles had led to excessive plastic deformation of the substrate. In the case of already bonded particles, the transferred peening energy of incoming particles had pushed them further into the soft Al alloy substrate.

The cross-sectional observations of Al 6082 T6 sample (Fig. 12b) indicated a deposit with inconsistent thickness of around 50–60 µm on a highly deformed substrate, confirming the low deposition efficiency of RCCA#1 powder. The first few deposited particles were mostly seen to have penetrated in the Al 6082 T6 substrate and become mechanically interlocked (Fig. 12b), acting as a new foundation for the subsequent impacting particles. The inherent hardness of the powder along with work hardening from peening effect of the successive impacting particles, could have cumulatively resulted in a harder platform for the subsequent layers to deposit. Comparable observations were reported in [44,45], where FeCoCrNiMn particles closer to the coating-substrate interface were reported to have experienced higher flattening and work hardening, due to the peening effect of successive particles.

CS on a Nimonic 75 substrate led to considerably lower deposition efficiency (Fig. 12c-e). Surface inspections revealed a few of initially interlocked RCCA#1 particles being consequently cracked and broken upon the impact of subsequent particles. Some of these particles may also have rebounded leaving large craters on the surface (Fig. 12c). The penetration depth of RCCA#1 particles on Nimonic 75 was lower compared to Al 6082 T6 substrate; loose embedment of the particles on Nimonic 75 seems to have favored their easier detachment and removal due to the impact of subsequent particles. This observation validates the proposed absence of metallurgical bonding between the particles and the substrate, as well as the relatively weak nature of the mechanical interlocking between them.

EBSD analysis was performed to further assess the deformation behavior of the particles cold sprayed on both substrates. Fig. 13a shows the investigated area of Al 6082 T6 substrate. The severe plastic deformation of the particles led to grain refinement, especially along the particle boundaries as seen in Fig. 13b. This inhomogeneous grain refinement is also evident from the Kernel average misorientation (KAM) maps presented in Fig. 13c. In comparison to the internal parts, the outer edges of the particles were severely strained. Previous CS studies have similarly identified dynamic recrystallization as the chief mechanism for grain refinement of the particles [27,29,46,47].

EBSD analysis on the Nimonic 75 substrate was performed on a representative zone of intermixing (Fig. 13d). Intrinsic features of CS deposits such as grain refinement through dynamic recrystallization were observed in Fig. 13d and e. A few linear substructures, which could be identified as shear bands or deformation twins were also observed in the entrapped particles (dashed black arrow at the bottom of Fig. 13e)

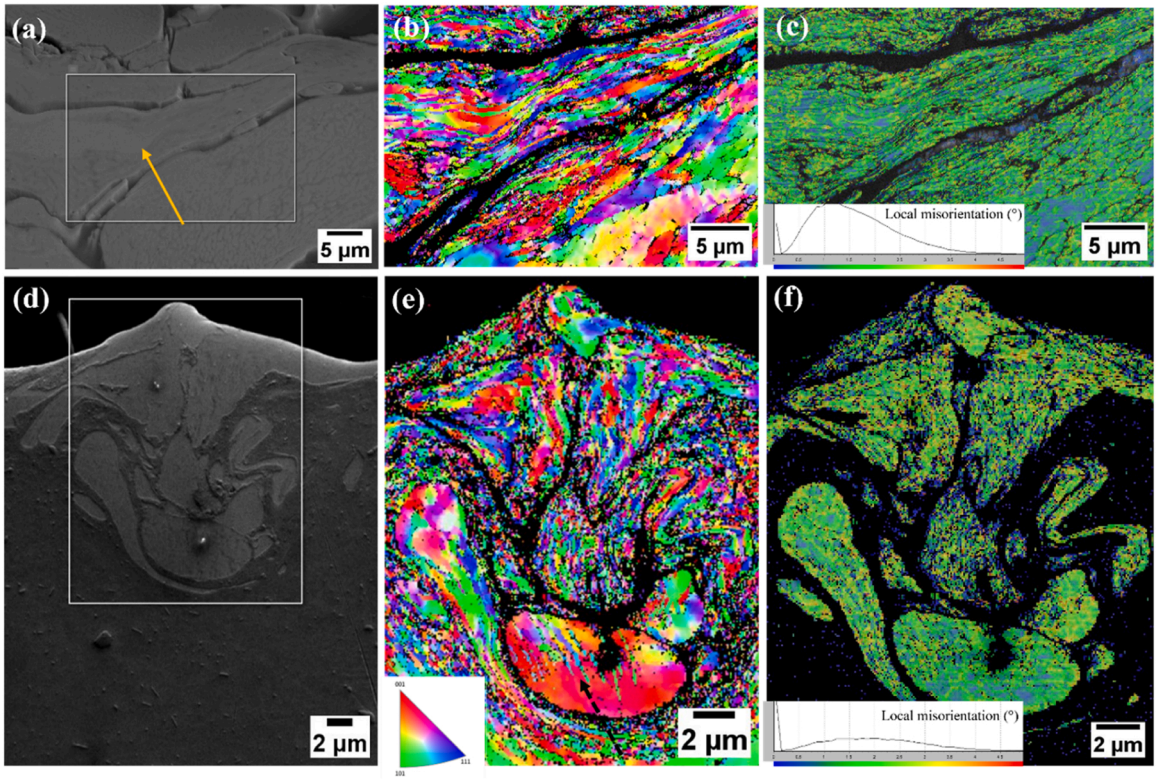

Fig. 13. (a) SEM image (yellow arrow pointing to the bulk area), (b) EBSD IPF, (c) KAM images of RCCA#1 deposited on Al 6082 T6 substrate. (d) SEM image (e) EBSD IPF and (f) KAM maps of the 'intermixing zone' formed in model RCCA#1 deposited on Nimonic 75.

due to the severe strain induced on these particles from multiple incoming impacts. High strain at low temperatures can induce deformation twins in the bcc metals [48,49]. The KAM map in Fig. 13f confirmed the higher strain in the entrapped particles compared to those superficially interlocked on the substrate.

As inferred from the elemental mapping of RCCA #1 particles presented in Section 2, a considerable number of particles possess enriched zones with comparably higher density of elements such as Ta and W. These zones also showed lower concentration of elements such as Ti and V, presence of which would have improved the ductility of the feedstock (Fig. 2). Interestingly, these zones, rich in Ta and W, were seen to be prevalent in the particles deposited on Al 6082 T6 substrates (yellow arrow in Fig. 13a), which were able to deform, as suggested by the misoriented subgrains in Fig. 13b. On the other hand, no such zones were observed in the deposits on Nimonic 75 substrates, which only had particles intermixed with the substrate material and consisting of uniformly dendritic grains. Hence, these Ta and W rich zones could not have withstood the energy of impact against harder Nimonic 75 substrates (277 ± 9 $HV_{1.0}$). Apart from this, the likely intrinsic brittleness of the particles due to higher oxygen and nitrogen content (refer Section 2) could also have affected the performance of the RCCA#1 feedstock upon impact [50–53].

5. Summary and discussion on the observed challenges

Characterization of the as-atomized RCCA#1 powder highlighted numerous challenges associated with pre-alloyed RCCA powder production, primarily including i) complete melting of the constituents with high-melting-points (e.g., W, Ta) to achieve a homogeneous melt, ii) the high sensitivity to oxygen and nitrogen impurity uptake during powder atomization that can lead to significant embrittlement, and iii) the wide particle size range. The latter is a particularly important issue for CS processing. These problems can directly affect the manufacturability and efficiency of the follow-on AM processes. For LPBF process, it is partially [54,55] possible to homogenize the composition by completely melting all the powder particles within the melt pool, which can be intensified by remelting strategies. However, in our study, the large melting point differences between the Ta/W rich areas and the rest of RCCA#1 composition impeded a full homogenization. For solid-state AM, the microstructural features are preserved in the build, and so do their related defects. There are reported studies indicating that, in the case of CS, pre-deposition heat treatments are able to address the inherent inhomogeneous microstructure of atomized powders that are not ideal for a treatment fully based on plastic deformation; various heat-treatments have been shown to promote particle deformability and deposition efficiency in CS [56,57].

Characterizations of the as-deposited LPBF and CS RCCA#1 samples highlighted the ensuing challenges in AM processing of RCCAs. LPBF features high residual stress accumulations due to large temperature gradients and high solidification rates in the melt pool. This results in the build quality being highly affected by thermal and stress management within the build [58] as well as alloy's sensitivity to thermal- and stress-induced cracking. RCCA#1 serves as a representative example demonstrating a combination of different sources of processability issues related to LPBF. Hot cracks are primarily induced by shrinkage strains when there is limited supply of liquid to the interdendritic regions at the later stage of solidification [41,59]. This is evident by a great number of entrapped pores at the interdendritic regions in Figs. 5c, 5d, as well as the dendritic structures observed at the fractured surfaces in Fig. 6b. As indicated by the Scheil solidification simulation curve in Fig. 3a, this model alloy is predicted to solidify across a wide temperature range (~850 K), which is 300 K higher than the predicted freezing range of C103, a commercial Nb-based diluted alloy with demonstrated good laser processability [60]. The large freezing range therefore tends to induce a larger area that is weak and susceptible to hot cracking [42,43]. Since the freezing range is composition-dependent, it guides the direction for RCCA alloy design and refinement for improved LPBF processability.

Based on the results of processing RCCA#1 with LPBF, another model alloy $Ta_1Nb_1V_1W_{0.25}Ti_{0.25}$ with minor Cr addition (hereafter referred to as RCCA#2) was created, aimed at achieving a reduced freezing range (less than 700 K as predicted in Fig. 14a) and potentially less Ti-segregation-induced phase instability. For rapid prototyping and comparison of laser processability, lab-scale arc-melted buttons were prepared from both RCCA#1 and RCCA#2 and multi-path laser scanning was carried on their polished surfaces. It is worth mentioning that literature reports much lower interstitial contents (e.g. ca. 160 ppm O and ca. 11 ppm N [61]) than in the powder used in this study. Furthermore, the samples created by arc-melting experiments also exhibited lower interstitial contents (O content < 1000 ppm). Comparison of laser treated surfaces of RCCA#1 (Fig. 14b) and RCCA#2 (Fig. 14c) demonstrates a very strong reduction of cracks that can be related to the improved alloy composition.

Further cross-sectional examination of the melt pool in laser-melted RCCA#2 also exhibited no hot tear cracks, and fine solidification microstructures without secondary dendrite arms that are visible at the micron-scale (Fig. 15a). This indicates better liquid feeding at the later stage of solidification preventing hot tearing. However, stress-induced cracks are still visible in some areas and the inter- and transcrystalline fractures at the fracture surface yet imply brittleness (Fig. 15b).

Although stress cracking remains the dominant phenomenon in LPBF builds, further chemical tweaking of the alloy combined with LPBF process optimization, including process parameters, preheating temperatures, and laser scanning strategies, are envisioned to minimize stress accumulation and reduce/prevent crack formation. While being promisingly effective in reducing crack density to less than 1 mm/mm^2, preheating the baseplate to 1000° C is not practically available in common commercial LPBF systems. Therefore, a dedicated custom tailoring and development of the LPBF system was undertaken at DLR to enable high baseplate temperature and small build space requiring much smaller powder volumes. Furthermore, measures should be taken to mitigate the significant Nitrogen pick-up at high temperatures, being another challenging aspect of HT-LPBF.

The identified challenge that remains to be addressed in the future work is related to the understanding of impurity uptake during powder production and LPBF process and its impact on the ductility of RCCAs. This requires methods for achieving reliable quantitative predictions that can serve for future RCCA alloy design and development.

CS experiments exhibited considerably low deposition efficiency and the dominance of mechanical interlocking and particle embedding, the extent of which was highly dependent on the relative hardness difference between the powder and the substrate material. This was evidenced by discontinuous deposits with maximum coating thickness ranging between 50 and 60 μm on Al 6082 T6 substrate, and relatively fewer particles mechanically embedded in the harder Nimonic 75 substrate. Wipe tests revealed mechanical interlocking to be the primary bonding mechanism on both substrates.

Besides the high oxygen content and limited ductility that can substantially affect the bonding probability in CS, the wide particle size distribution also had a notable detrimental effect on the deposition efficiency. The mean particle size was measured to be 7.19 μm (considering 20,000 particles) with around 90 % of the particles measuring below 16 μm. Under the given processing conditions, smaller particles might gain higher velocity for a given set of CS process parameters, owing to their lower mass [22]. Their high impact velocity could have been high enough to surpass the upper threshold of deposition window and result in substrate erosion, as evident by the intense amount of deformation observed on both substrates. Therefore, the feedstock's particle size distribution could also be contributing to the lower deposition efficiency of RCCA#1 on both substrates. In the case of RCCA#1 sprayed on Al 6082 T6, there was no significant change in the thickness after deposition. However, RCCA#1 sprayed on Nimonic 75 resulted in considerable reduction in the thickness of the substrate. This observation indicates that the lower stand-off distance, compared to the spray trials with Al 6082 T6 substrate, could be contributing to the exacerbated substrate erosion.

There exist studies, which suggest sieving as a possible solution to address the skewed powder size distribution in the CS feedstock [62,63]. However, it is to be noted that when the particles are brittle and characterized with a significant number of satellites, as in case of this study, it is plausible that the kinetic energy transferred to particles during their supersonic acceleration and in-flight impacts, may result in separation of the small satellites with brittle connection to the parent particles, resulting in the re-emergence of the wide particle size distribution before impact.

Cross-section and the surface morphology of the CS deposits clearly revealed the presence of zones where the powder material and substrate material seemed to be mixed. Similar observations were reported in other CS studies highlighting the significance of low deposition efficiency (continuous peening and rebounding), and the relatively high difference in the mechanical properties of the powder and the substrate in the formation of this intermixing zones [64]. This observation was more pronounced on Nimonic 75 substrate compared to Al 6082 (See Figs. 11b, 11e). This could be attributed to the considerably lower hardness of the Al 6082 T6 substrate (104 ± 2 $HV_{1.0}$) compared to the Nimonic 75, and consequent higher hardness difference with respect to RCCA#1 particles (502 ± 38 $HV_{0.025}$); the higher deformation of the Al 6082 T6 substrate compared to that of Nimonic 75, could have reduced the amount of shear stresses generated inside the particle upon impact. The postulated mechanism for these powder-substrate intermixing zones [64] based on the experimental observations on both substrates is presented in Fig. 16 and described below.

The initial powder particles impacting the substrate get mechanically interlocked to the substrate, resulting in a small outward jetting of the

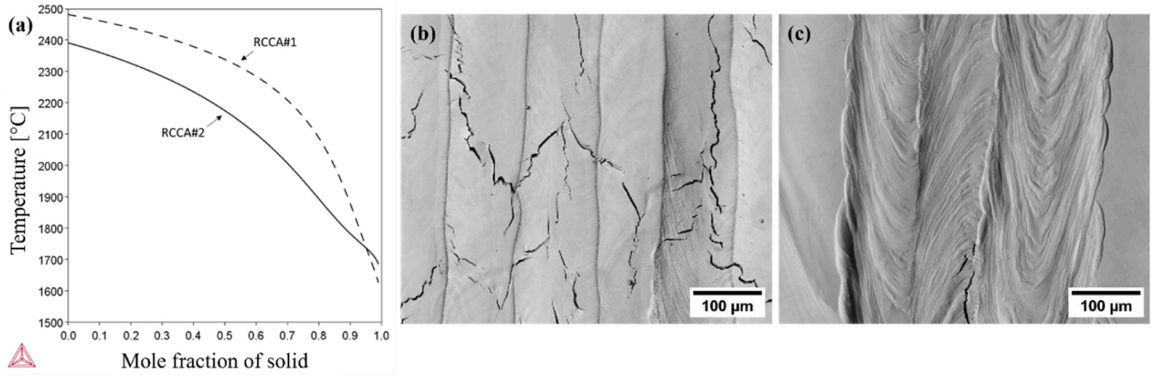

Fig. 14. (a) Classic Scheil simulation of RCCA#2. (b) Surface of an arc-melted button of RCCA#1 after laser scanning. (c) Surface of an arc-melted button of RCCA#2 after laser scanning.

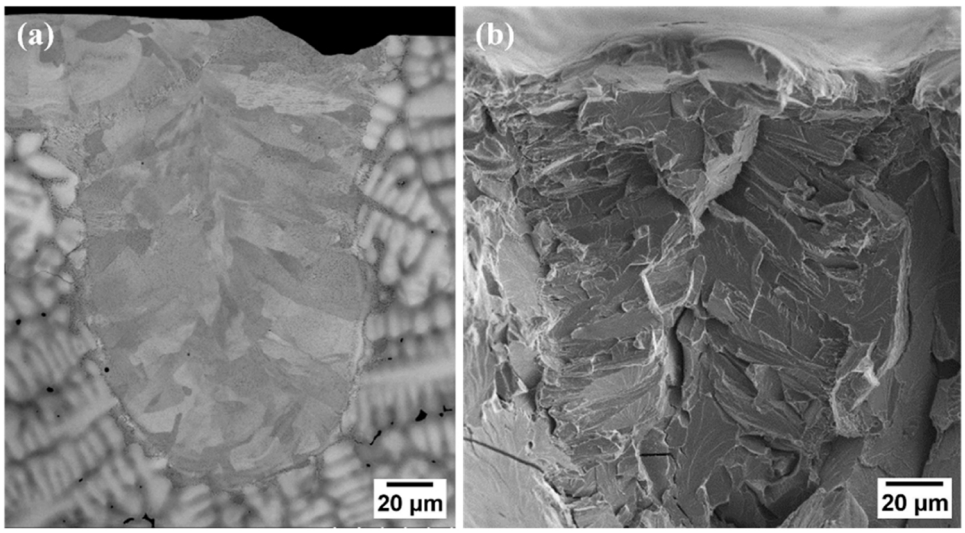

Fig. 15. (a) SEM Cross-section of the melt pool structure after laser scanning trial on the surface of an arc-melted button of RCCA#2; (b) Fracture surface morphology of the melt pool of RCCA#2.

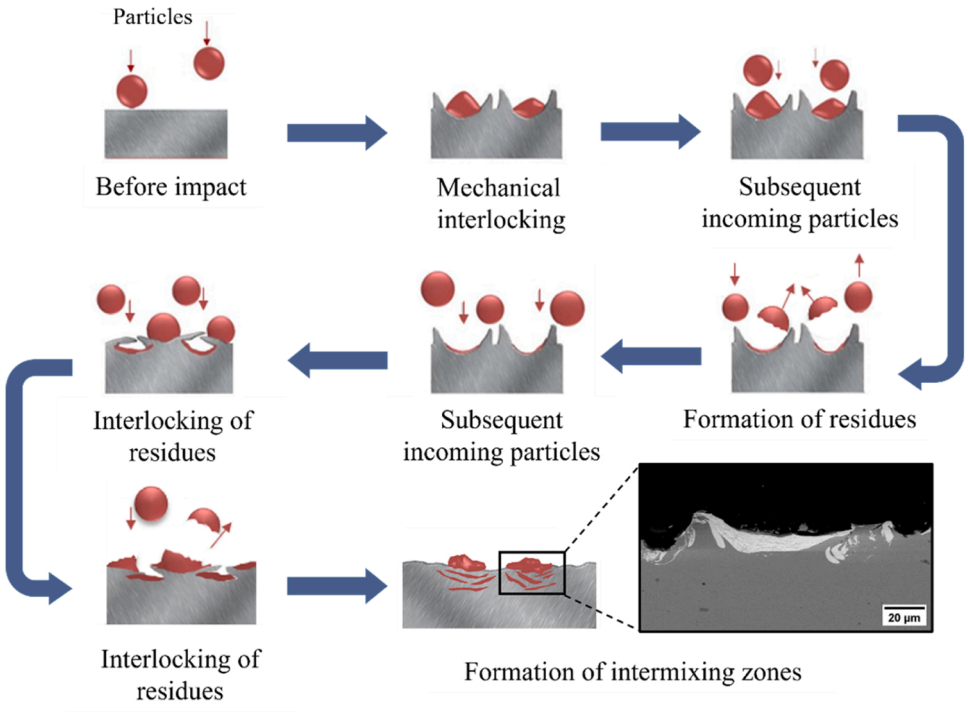

Fig. 16. Schematic representation on formation of intermixing zones during CS deposition of RCCA#1 particles on Nimonic 75 substrate.

substrate. The subsequent particles impact and crack the already deposited ones. Owing to their brittleness and weak bonding to the substrate, some particle debris fly away due to the impact, while some land on the surface. The residuals laid on the surface together with the outward sheared substrate jetting get impacted by the subsequently incoming particles and get flattened and eventually embedded. They are further pushed inside the substrate, generating internal shear stresses, which can further promote internal fracture and thus generate separations in the intermixed layer. This sequence is continuously repeated during spraying, leading to the formation of the 'intermixing zone'.

Moreover, particles retained in deposits on Al 6082 T6 substrate had larger Ta rich zones, whereas on Nimonic 75, the few deposited particles showed similar chemical composition to that of the feedstock with no sign of Ta rich zones. This suggests that the presence of high concentrations of Ta, W, and reduction in the concentrations of V and Ti in these larger grains could have affected the powder ductility and resulted in reduced deposition.

We postulate that the low deformability of the RCCA power under study can be compensated by either enhancing the mechanical interlocking as the prominent adhesion mechanism or increasing the velocity and therefore the kinetic energy of the impacting particles. Based on available studies, the first approach can be achieved by promoting thermal softening of the substrate through laser-assisted cold spray (LACS) [65]. This approach has been demonstrated to increase the deposition efficiency and enhance coating characteristics of particularly hard feedstock, including the HEAs [66], Ti [67], Ti64[68] and various alloys of steel [67,69]. In addition, assuming a more deformable RCCA achievable through further manufacturing adjustments and

modifications, higher particle velocity can enhance the sprayability of the feedstock. This can be realized by employing He as the process gas for CS, facilitating the acceleration of particles to higher velocities [70].

6. Conclusions and future perspectives

Several critical challenges have been summarized and elucidated with respect to pre-alloyed refractory complex concentrated alloy powder production and additive manufacturing processing via laser powder bed fusion and cold spray. Analysis of the experimental observations results in the following guidelines and recommendations for design and processing of refractory complex concentrate alloys:

- Controlled powder quality in terms of homogeneous microstructure, uniform chemical concentration, higher purity, and possibly a narrower particle size distribution (the latter especially significant in the case of cold spray processing) would increase the processability and the build quality of the refractory complex concentrate alloy material.
- Where possible, prioritizing sufficient, medium to low-temperature ductility over other properties, i.e., by means of increasing the alloy's tolerance to interstitial oxygen and nitrogen is critical in RCCA alloy design. This requires more fundamental scientific research for understanding the interactions between interstitial and refractory atoms. Moreover, the impacts of these parameters on materials fracture behaviors should be also analyzed to provide guidance for engineering-oriented material model development and reliable predictions of impurity uptake during powder production and laser processing, and its effects on strength/ductility trade-off.
- For laser processing, additional chemical modification should be considered for less sensitivity to hot cracking, such as minimized freezing range to prevent hot tearing cracks. Hybrid optimization of laser processing conditions and scanning strategies allow for improved homogenization of the melt pool and minimized extrinsic defects and cracks, further improving the build quality. However, it may be at the cost of the fabrication efficiency.
- The cold spray deposition efficiency could be further improved by spraying at higher gas stagnation temperature and pressure, use of Helium instead of Nitrogen as the process gas, and implementation of possible in-situ treatments like laser-assisted cold spray (to heat the particle flow during impact). These treatments could promote softening and oxide layer breakage, facilitating a metallurgical bond between the powder particles. However, the associated additional process cost and sustainability issues should be carefully evaluated.

Overall, this study led to the identification of significant bottlenecks during the development and deployment of this challenging class of novel high-temperature materials. In particular, considering powder manufacturing, high prioritization of requirements for later processing technologies in the early stages of alloy design was found to be essential. With these lessons the challenges in RCCA alloy developments and modifications may be resolved more quickly or avoided altogether in the future.

CRediT authorship contribution statement

Magesh Kumaravel: Writing – original draft, Visualization, Validation, Investigation, Formal analysis. **Joachim Gussone:** Writing – original draft, Visualization, Methodology, Investigation, Formal analysis. **Yazdan Eynolghozzat:** Writing – original draft, Visualization, Investigation. **Amir Ardeshiri Lordejani:** Writing – review & editing, Methodology, Investigation. **Fuyao Yan:** Writing – original draft, Visualization, Investigation, Formal analysis, Data curation. **Guillermo Raquena:** Writing – review & editing, Methodology, Data curation. **Jan Haubrich:** Writing – review & editing, Methodology, Formal analysis. **Mario Guagliano:** Writing – review & editing, Supervision, Resources, Project administration, Methodology. **Ida Berglund:** Writing – review & editing, Supervision, Methodology. **Sara Bagherifard:** Writing – review & editing, Supervision, Methodology, Conceptualization.

Declaration of Competing Interest

The authors declare that they have no known competing financial interests or personal relationships that could have appeared to influence the work reported in this paper.

Data Availability

Data will be made available on request.

Acknowledgement

The research leading to these results has received funding from the European Union's Horizon 2020 programme for research and innovation under grant agreement no. 101004172 (ATLAS, Advanced Design of High Entropy Alloys Based Materials for Space Propulsion).

References

[1] O.N. Senkov, D.B. Miracle, K.J. Chaput, J.P. Couzinie, Development and exploration of refractory high entropy alloys - a review, J. Mater. Res 33 (2018) 3092–3128, https://doi.org/10.1557/jmr.2018.153.
[2] J.H. Perepezko, The hotter the engine, the better, Science 326 (1979) (2009) 1067–1068, https://doi.org/10.1126/science.1179117.
[3] N. Zubair, N. Ejaz, M. Mansoor, Oxidation resistant nickel aluminide coating on niobium alloy C103 for high temperature aerospace applications, Solid State Phenom. 336 (2022) 43–48, https://doi.org/10.4028/p-g44bm8.
[4] B. Blakey-Milner, P. Gradl, G. Snedden, M. Brooks, J. Pitot, E. Lopez, M. Leary, F. Berto, A. du Plessis, Metal additive manufacturing in aerospace: a review, Mater. Des. 209 (2021), https://doi.org/10.1016/j.matdes.2021.110008.
[5] O.N. Senkov, G.B. Wilks, J.M. Scott, D.B. Miracle, Mechanical properties of Nb25Mo25Ta 25W25 and V20Nb20Mo 20Ta20W20 refractory high entropy alloys, Intermet. (Barking) 19 (2011) 698–706, https://doi.org/10.1016/j.intermet.2011.01.004.
[6] O.N. Senkov, J.M. Scott, S.V. Senkova, D.B. Miracle, C.F. Woodward, Microstructure and room temperature properties of a high-entropy TaNbHfZrTi alloy, J. Alloy. Compd. 509 (2011) 6043–6048, https://doi.org/10.1016/j.jallcom.2011.02.171.
[7] C. Lee, D. Xie, B. Kyle Derby, J. Kevin Baldwin, C. Tandoc, O. Ei Atwani, Y.J. Hu, J. A. Valdez, N. Li, S.J. Fensin, An experimentally driven high-throughput approach to design refractory high-entropy alloys, Mater. Des. 223 (2022), https://doi.org/10.1016/j.matdes.2022.111259.
[8] R. Feng, C. Zhang, M.C. Gao, Z. Pei, F. Zhang, Y. Chen, D. Ma, K. An, J. D. Poplawsky, L. Ouyang, Y. Ren, J.A. Hawk, M. Widom, P.K. Liaw, High-throughput design of high-performance lightweight high-entropy alloys, Nat. Commun. 12 (2021), https://doi.org/10.1038/s41467-021-24523-9.
[9] O.N. Senkov, J.D. Miller, D.B. Miracle, C. Woodward, Accelerated exploration of multi-principal element alloys with solid solution phases, Nat. Commun. 6 (2015), https://doi.org/10.1038/ncomms7529.
[10] L.L. Snead, D.T. Hoelzer, M. Rieth, A.A.N. Nemith, Refractory Alloys: Vanadium, niobium, molybdenum, tungsten. Structural Alloys for Nuclear Energy Applications, Elsevier, 2019, pp. 585–640, https://doi.org/10.1016/B978-0-12-397046-6.00013-7.
[11] T.G. Nieh, J. Wadsworth, Recent Advances and Developments in Refractory Alloys, MRS Online Proc. Libr. 322 (1993) 315–327, https://doi.org/10.1557/PROC-322-315.
[12] H.W. Yao, J.W. Qiao, J.A. Hawk, H.F. Zhou, M.W. Chen, M.C. Gao, Mechanical properties of refractory high-entropy alloys: Experiments and modeling, J. Alloy. Compd. 696 (2017) 1139–1150, https://doi.org/10.1016/j.jallcom.2016.11.188.
[13] H. Dobbelstein, M. Thiele, E.L. Gurevich, E.P. George, A. Ostendorf, Direct metal deposition of refractory high entropy alloy MoNbTaW, in: Phys Procedia, Elsevier B.V., 2016, pp. 624–633, https://doi.org/10.1016/j.phpro.2016.08.065.
[14] H. Dobbelstein, E.L. Gurevich, E.P. George, A. Ostendorf, G. Laplanche, Laser metal deposition of a refractory TiZrNbHfTa high-entropy alloy, Addit. Manuf. 24 (2018) 386–390, https://doi.org/10.1016/j.addma.2018.10.008.
[15] M.A. Melia, S.R. Whetten, R. Puckett, M. Jones, M.J. Heiden, N. Argibay, A. B. Kustas, High-throughput additive manufacturing and characterization of refractory high entropy alloys, Appl. Mater. Today 19 (2020), https://doi.org/10.1016/j.apmt.2020.100560.
[16] H. Dobbelstein, E.L. Gurevich, E.P. George, A. Ostendorf, G. Laplanche, Laser metal deposition of compositionally graded TiZrNbTa refractory high-entropy alloys using elemental powder blends, Addit. Manuf. 25 (2019) 252–262, https://doi.org/10.1016/j.addma.2018.10.042.

[17] F. Huber, D. Bartels, M. Schmidt, In situ alloy formation of a wmotanbv refractory metal high entropy alloy by laser powder bed fusion (Pbf-lb/m), Materials 14 (2021), https://doi.org/10.3390/ma14113095.
[18] T. Ron, A. Leon, V. Popov, E. Strokin, D. Eliezer, A. Shirizly, E. Aghion, Synthesis of Refractory High-Entropy Alloy WTaMoNbV by Powder Bed Fusion Process Using Mixed Elemental Alloying Powder, Materials 15 (2022), https://doi.org/10.3390/ma15124043.
[19] H. Zhang, Y. Zhao, S. Huang, S. Zhu, F. Wang, D. Li, Manufacturing and analysis of high-performance refractory high-entropy alloy via selective laser melting (SLM), Materials 12 (2019), https://doi.org/10.3390/ma12050720.
[20] D. Bourell, J.P. Kruth, M. Leu, G. Levy, D. Rosen, A.M. Beese, A. Clare, Materials for additive manufacturing, CIRP Ann. Manuf. Technol. 66 (2017) 659–681, https://doi.org/10.1016/j.cirp.2017.05.009.
[21] G.N. Devi, A.V. Gopal, S. Kumar, Investigations on inter-splat boundaries of cold sprayed Ni–Cr coatings upon high temperature oxidation, Surf. Coat. Technol. 467 (2023), https://doi.org/10.1016/j.surfcoat.2023.129691.
[22] T. Schmidt, F. Gärtner, H. Assadi, H. Kreye, Development of a generalized parameter window for cold spray deposition, Acta Mater. 54 (2006) 729–742, https://doi.org/10.1016/j.actamat.2005.10.005.
[23] T. Ishimoto, R. Ozasa, K. Nakano, M. Weinmann, C. Schnitter, M. Stenzel, A. Matsugaki, T. Nagase, T. Matsuzaka, M. Todai, H.S. Kim, T. Nakano, Development of TiNbTaZrMo bio-high entropy alloy (BioHEA) super-solid solution by selective laser melting, and its improved mechanical property and biocompatibility, Scr. Mater. 194 (2021), https://doi.org/10.1016/j.scriptamat.2020.113658.
[24] F. Yan, W. Xiong, E. Faierson, G.B. Olson, Characterization of nano-scale oxides in austenitic stainless steel processed by powder bed fusion, Scr. Mater. 155 (2018) 104–108, https://doi.org/10.1016/j.scriptamat.2018.06.011.
[25] B. Barnett, M. Trexler, V. Champagne, Cold sprayed refractory metals for chrome reduction in gun barrel liners, Int J. Refract Met. Hard Mater. 53 (2015) 139–143, https://doi.org/10.1016/j.ijrmhm.2015.07.007.
[26] J. Mahaffey, A. Vackel, S. Whetten, M. Melia, A.B. Kustas, Structure Evolution and Corrosion Performance of CoCrFeMnNi High Entropy Alloy Coatings Produced Via Plasma Spray and Cold Spray, J. Therm. Spray. Technol. 31 (2022) 1143–1154, https://doi.org/10.1007/s11666-022-01373-5.
[27] S. Yin, W. Li, B. Song, X. Yan, M. Kuang, Y. Xu, K. Wen, R. Lupoi, Deposition of FeCoNiCrMn high entropy alloy (HEA) coating via cold spraying, J. Mater. Sci. Technol. 35 (2019) 1003–1007, https://doi.org/10.1016/j.jmst.2018.12.015.
[28] R. Nikbakht, M. Saadati, T.S. Kim, M. Jahazi, H.S. Kim, B. Jodoin, Cold spray deposition characteristic and bonding of CrMnCoFeNi high entropy alloy, Surf. Coat. Technol. 425 (2021), https://doi.org/10.1016/j.surfcoat.2021.127748.
[29] Y. Xu, W. Li, L. Qu, X. Yang, B. Song, R. Lupoi, S. Yin, Solid-state cold spraying of FeCoCrNiMn high-entropy alloy: an insight into microstructure evolution and oxidation behavior at 700-900 °C, J. Mater. Sci. Technol. 68 (2021) 172–183, https://doi.org/10.1016/j.jmst.2020.06.041.
[30] D.F. Rojas, H. Li, O.K. Orhan, C. Shao, J.D. Hogan, M. Ponga, Mechanical and microstructural properties of a CoCrFe0.75NiMo0.3Nb0.125 high-entropy alloy additively manufactured via cold-spray, J. Alloy. Compd. 893 (2022), https://doi.org/10.1016/j.jallcom.2021.162309.
[31] A. Anupam, S. Kumar, N.M. Chavan, B.S. Murty, R.S. Kottada, First report on cold-sprayed AlCoCrFeNi high-entropy alloy and its isothermal oxidation, J. Mater. Res 34 (2019) 796–806, https://doi.org/10.1557/jmr.2019.38.
[32] J. Liu, K. Ma, Y. Ding, L. Feng, W. Li, L. Li, Microstructure and Properties of an FeCoCrAlCu HEA Coating Synthesized via the Induction Remelting Method, Coatings 13 (2023), https://doi.org/10.3390/coatings13020399.
[33] L. Feng, W.J. Yang, K. Ma, Y.D. Yuan, G.S. an, W.S. Li, Microstructure and Properties of Cold Spraying AlCoCrCuFeNix HEA Coatings Synthesized by Induction Remelting, Mater. Technol. 37 (2022) 2567–2579, https://doi.org/10.1080/10667857.2022.2046929.
[34] D.V. Hushchyk, A.I. Yurkova, V.V. Cherniavsky, I.I. Bilyk, S.O. Nakonechnyy, Nanostructured AlNiCoFeCrTi high-entropy coating performed by cold spray, Appl. Nanosci. (Switz.) 10 (2020) 4879–4890, https://doi.org/10.1007/s13204-020-01364-4.
[35] J.-O. Anderson, T. Helander, L. Höglund, P. Shi, B. Sundman, THERMO-CALC & DICTRA, Computational Tools for Material Science, Calphad 26 (2002) 273–312.
[36] Thermo-Calc Software TCHEA High Entropy Alloy Database version 6, (n.d.).
[37] C.H. Belcher, B.E. MacDonald, D. Apelian, E.J. Lavernia, The role of interstitial constituents in refractory complex concentrated alloys, Prog. Mater. Sci. 137 (2023), https://doi.org/10.1016/j.pmatsci.2023.101140.
[38] A. Simchi, H. Pohl, Effects of laser sintering processing parameters on the microstructure and densification of iron powder, Mater. Sci. Eng.: A 359 (2003) 119–128, https://doi.org/10.1016/S0921-5093(03)00341-1.
[39] M.C. Flemings, Solidification Processing, McGraw Hill, New York, 1974.
[40] J. Cambell, Castings, Second, Butterworth Heinemann, Oxford, 2003.
[41] M. Rappaz, J.-M. Drezet, M. Gremaud, A N. Hot-Tearing Criterion (1999).
[42] Y.T. Tang, C. Panwisawas, J.N. Ghoussoub, Y. Gong, J.W.G. Clark, A.A.N. Németh, D.G. McCartney, R.C. Reed, Alloys-by-design: Application to new superalloys for additive manufacturing, Acta Mater. 202 (2021) 417–436, https://doi.org/10.1016/j.actamat.2020.09.023.
[43] Z. Sun, X.P. Tan, M. Descoins, D. Mangelinck, S.B. Tor, C.S. Lim, Revealing hot tearing mechanism for an additively manufactured high-entropy alloy via selective laser melting, Scr. Mater. 168 (2019) 129–133, https://doi.org/10.1016/j.scriptamat.2019.04.036.
[44] P. Cavaliere, A. Perrone, A. Silvello, A. Laska, G. Blasi, I.G. Cano, B. Sadeghi, S. Nagy, Cyclic behavior of FeCoCrNiMn high entropy alloy coatings produced through cold spray, J. Alloy. Compd. 931 (2023), https://doi.org/10.1016/j.jallcom.2022.167550.
[45] H. Assadi, T. Schmidt, H. Richter, J.O. Kliemann, K. Binder, F. Gärtner, T. Klassen, H. Kreye, On parameter selection in cold spraying, J. Therm. Spray. Technol. 20 (2011) 1161–1176, https://doi.org/10.1007/s11666-011-9662-9.
[46] R.B. Nair, G. Perumal, A. McDonald, Effect of Microstructure on Wear and Corrosion Performance of Thermally Sprayed AlCoCrFeMo High-Entropy Alloy Coatings, Adv. Eng. Mater. 24 (2022), https://doi.org/10.1002/adem.202101713.
[47] R.B. Nair, S. Ngan, A. McDonald, Dry abrasive wear and solid particle erosion assessments of high entropy alloy coatings fabricated by cold spraying, Mater. Today Commun. 34 (2023), https://doi.org/10.1016/j.mtcomm.2023.105527.
[48] X. Li, Z. Zhang, J. Wang, Deformation twinning in body-centered cubic metals and alloys, Prog. Mater. Sci. 139 (2023), https://doi.org/10.1016/j.pmatsci.2023.101160.
[49] I.J. Beyerlein, X. Zhang, A. Misra, Growth twins and deformation twins in metals, Annu Rev. Mater. Res 44 (2014) 329–363, https://doi.org/10.1146/annurev-matsci-070813-113304.
[50] L. Shao, M. Yang, L. Ma, B.Y. Tang, Effect of Ta and Ti content on high temperature elasticity of HfNbZrTa1−xTix refractory high-entropy alloys, Int J. Refract Met. Hard Mater. 95 (2021), https://doi.org/10.1016/j.ijrmhm.2020.105451.
[51] Z.D. Han, H.W. Luan, X. Liu, N. Chen, X.Y. Li, Y. Shao, K.F. Yao, Microstructures and mechanical properties of TixNbMoTaW refractory high-entropy alloys, Mater. Sci. Eng.: A 712 (2018) 380–385, https://doi.org/10.1016/j.msea.2017.12.004.
[52] M. Wang, Z.L. Ma, Z.Q. Xu, X.W. Cheng, Effects of vanadium concentration on mechanical properties of VxNbMoTa refractory high-entropy alloys, Mater. Sci. Eng.: A 808 (2021), https://doi.org/10.1016/j.msea.2021.140848.
[53] B. Yin, F. Maresca, W.A. Curtin, Vanadium is an optimal element for strengthening in both fcc and bcc high-entropy alloys, Acta Mater. 188 (2020) 486–491, https://doi.org/10.1016/j.actamat.2020.01.062.
[54] H. Li, E.G. Brodie, C. Hutchinson, Predicting the chemical homogeneity in laser powder bed fusion (LPBF) of mixed powders after remelting, Addit. Manuf. 65 (2023), https://doi.org/10.1016/j.addma.2023.103447.
[55] F. Bosio, D. Manfredi, M. Lombardi, Homogenization of an Al alloy processed by laser powder bed fusion in-situ alloying, J. Alloy. Compd. 904 (2022), https://doi.org/10.1016/j.jallcom.2022.164079.
[56] W.A. Story, L.N. Brewer, Heat Treatment of Gas-Atomized Powders for Cold Spray Deposition, Met. Mater. Trans. A Phys. Met. Mater. Sci. 49 (2018) 446–449, https://doi.org/10.1007/s11661-017-4428-8.
[57] A. Sabard, H.L. de Villiers Lovelock, T. Hussain, Microstructural Evolution in Solution Heat Treatment of Gas-Atomized Al Alloy (7075) Powder for Cold Spray, J. Therm. Spray. Technol. 27 (2018) 145–158, https://doi.org/10.1007/s11666-017-0662-2.
[58] N.C. Levkulich, S.L. Semiatin, J.E. Gockel, J.R. Middendorf, A.T. DeWald, N. W. Klingbeil, The effect of process parameters on residual stress evolution and distortion in the laser powder bed fusion of Ti-6Al-4V, Addit. Manuf. 28 (2019) 475–484, https://doi.org/10.1016/j.addma.2019.05.015.
[59] D.G. Eskin, Suyitno, L. Katgerman, Mechanical properties in the semi-solid state and hot tearing of aluminium alloys, Prog. Mater. Sci. 49 (2004) 629–711, https://doi.org/10.1016/S0079-6425(03)00037-9.
[60] P.D. Awasthi, P. Agrawal, R.S. Haridas, R.S. Mishra, M.T. Stawovy, S. Ohm, A. Imandoust, Mechanical properties and microstructural characteristics of additively manufactured C103 niobium alloy, Mater. Sci. Eng.: A 831 (2022), https://doi.org/10.1016/j.msea.2021.142183.
[61] R.J. Scales, D.E.J. Armstrong, A.J. Wilkinson, B.S. Li, On the brittle-to-ductile transition of the as-cast TiVNbTa refractory high-entropy alloy, Mater. (Oxf.) 14 (2020), https://doi.org/10.1016/j.mtla.2020.100940.
[62] S. Kumar, B.R. Bodapati, G. Vinay, K. Vamshi Kumar, N.M. Chavan, P. Suresh Babu, A. Jyothirmayi, Estimation of inter-splat bonding and its effect on functional properties of cold sprayed coatings, Surf. Coat. Technol. 420 (2021), https://doi.org/10.1016/j.surfcoat.2021.127318.
[63] B. Jodoin, L. Ajdelsztajn, E. Sansoucy, A. Zúñiga, P. Richer, E.J. Lavernia, Effect of particle size, morphology, and hardness on cold gas dynamic sprayed aluminum alloy coatings, Surf. Coat. Technol. 201 (2006) 3422–3429, https://doi.org/10.1016/j.surfcoat.2006.07.232.
[64] S. Yin, J. Cizek, J. Cupera, M. Hassani, X. Luo, R. Jenkins, Y. Xie, W. Li, R. Lupoi, Formation conditions of vortex-like intermixing interfaces in cold spray, Mater. Des. 200 (2021), https://doi.org/10.1016/j.matdes.2020.109444.
[65] D. K, M. Jeandin, E. Irissou, J.-G. Legoux, W. Knapp, Laser-Assisted Cold Spray (LACS). in: Nd YAG Laser, InTech, 2012, https://doi.org/10.5772/36104.
[66] R. Nikbakht, C.V. Cojocaru, M. Aghasibeig, É. Irissou, T.S. Kim, H.S. Kim, B. Jodoin, Cold Spray and Laser-Assisted Cold Spray of CrMnCoFeNi High Entropy Alloy Using Nitrogen as the Propelling Gas, J. Therm. Spray. Technol. 31 (2022) 1129–1142, https://doi.org/10.1007/s11666-022-01361-9.
[67] M. Bray, A. Cockburn, W. O'Neill, The Laser-assisted Cold Spray process and deposit characterisation, Surf. Coat. Technol. 203 (2009) 2851–2857, https://doi.org/10.1016/j.surfcoat.2009.02.135.
[68] A.M. Birt, V.K. Champagne, R.D. Sisson, D. Apelian, Statistically Guided Development of Laser-Assisted Cold Spray for Microstructural Control of Ti-6Al-4V, Met. Mater. Trans. A Phys. Met. Mater. Sci. 48 (2017) 1931–1943, https://doi.org/10.1007/s11661-017-3970-8.
[69] D.J. Barton, V.S. Bhattiprolu, G.B. Thompson, L.N. Brewer, Laser assisted cold spray of AISI 4340 steel, Surf. Coat. Technol. 400 (2020), https://doi.org/10.1016/j.surfcoat.2020.126218.
[70] D.L. Gilmore, R.C. Dykhuizen, R.A. Neiser, T.J. Roemer, M.F. Smith, Particle Velocity and Deposition Efficiency in the Cold Spray Process, n.d.